The effect of shear-thickening on liquid transfer from an idealized gravure cell

Sunilkumar Khandavalli[a], J. Alex Lee[b], Matteo Pasquali[b,c], Jonathan P. Rothstein[*,a]

[a] *Mechanical and Industrial Engineering, University of Massachusetts Amherst, MA 01003 USA*
[b] *Chemical and Biomolecular Engineering, Rice University, Houston, TX 77005 USA*
[c] *Department of Chemistry, Ken Kennedy Institute for Information Technology, and The Smalley Institute for Nanoscale Science & Technology, Rice University, Houston, TX, 77005. USA*

Abstract

Gravure printing is an economical roll-to-roll processing technique with potential to revolutionize the fabrication of nano-patterned thin films at high throughput. In the present study, we investigated the impact of shear-thickening on the liquid transfer from an idealized gravure cell by a combination of experiments and numerical computations. We chose as a model system fumed silica nanoparticles dispersed in polypropylene glycol; these dispersions exhibit shear and extensional thickening as verified by steady shear and filament stretching extensional rheometry. Model gravure printing experiments were conducted using a linear motor to pick out the fluid vertically up from a truncated conical shaped idealized gravure cell cavity; the cell size is large enough that gravity is important, and therefore experiments were also conducted to pickout the fluid vertically down from the cavity-on-top. The amount liquid transfer from the cavity was studied with varying stretch velocities and dispersion concentrations. The filament profile evolution during the pickout process was examined using a high speed camera. Beyond a critical stretch rate, shear-thickening of the fluid, manifested by the formation of long stable filaments, exacerbates gravitational drainage during pickout. Beyond a second critical stretch rate, shear-thinning induces conical profile evolutions that result in pickout insensitive to stretch rate. All of these observations were qualitatively predicted by finite element computations using a generalized Newtonian fluid model, where the shear rheology was modeled explicitly. We showed that under the influence of gravity, wetting/de-wetting may be a critical phenomenon in determining pickout at low stretch rates.

Keywords: Gravure printing, Coating, Shear thickening, Colloids, Filament stretching,

[*]Corresponding author at: Mechanical and Industrial Engineering, University of Massachusetts Amherst, MA 01003 USA, Tel.:+1 413 577 0110; fax: +1 413 545 1027

Email address: rothstein@ecs.umass.edu (Jonathan P. Rothstein[*,])

1 Introduction

Roll-roll coating and printing of flexible substrates is a technology of great industrial and commercial importance due to its low cost and high throughput [1, 2]. This technology enables the fabrication of thin organic, inorganic and mixed organic/inorganic films with nanoscale patterns at high resolution for devices in wide applications such as, solar cells, thin film transistors, organic light emitting diodes, biosensors and biodevices [3, 4, 5, 6, 7, 8]. Gravure printing is a roll-roll processing technique used to coat/print thin films less than 50 μm for a wide variety of applications in high volumes such as magazines, packaging, flexible electronics, greeting cards and tapes [9, 10, 11, 12]. In gravure process, a roller with desired engraving, typically in microns dimensions, is passed through an ink reservoir and the excess is metered off by passing by a doctor blade. The ink from the cavities is then deposited on to the substrate held by another roller at high speeds (up to 15 mm/s).

During the ink transfer process, a liquid bridge is formed and stretched between the gravure cell (the cavity) and web, as the ink is deposited onto the substrate. The liquid bridge experiences complex kinematics; a combination of shear and extension due to relative motion between the gravure cell and web [13, 14]. The stability and breakup dynamics of the liquid bridge during the ink transfer can significantly affect the quality of the print or coated film. Partial emptying of the cavities or the formation of satellite drops can negatively impact the quality and the efficiency of the printing process [15]. Including gravure printing, the dynamics of the liquid bridge are strongly relevant in other applications such as contact drop dispensing [16], float-zone crystallization [17] and oil recovery [18]. Therefore, the dynamics, stability and breakup of the liquid bridge have been widely studied [16, 18, 19, 20, 21, 22]. Numerous studies, both experimental and numerical, have been performed to better understand the dynamics of a liquid bridge uniaxially stretched between two flat plates [23, 24, 25], as well between a flat plate and a cavity [26, 27, 28, 29]. There have also been numerical and experimental studies on ink transfer behavior in gravure printing considering pure shear [30, 31, 32], a combination of shear and extensional motion of the liquid bridge [33, 34], as well as studies which considering the effect of the rotation of the gravure cavity as the liquid is applied to the moving web by the rotating gravure roller [34, 13].

Printing fluids often are non-Newtonian, as many inks contain large concentrations of particles and polymer additives [35, 7, 12]. Only recently have any studied reported on the behavior of non-Newtonian fluids during gravure printing. Huang et al. [29] performed numerical computations using volume of fluid (VOF) method to examine the break up dynamics of shear-thinning fluids. They observed a fast break up of the filament and the formation of more satellite drops for the case of shear-thinning fluids compared to Newtonian fluids. Ahmed et al. [36] employed numerical computations to investigate the ink transfer behavior of shear-thinning fluids between two flat plates. They examined the influence of inertia, surface tension and top plate contact angle on the ink transfer ratio. Numerical computations on a shear-thinning fluid by Ghadiri et al. [37] showed that factors such as groove angle, groove depth and wettability can have significant impact on the filament dynamics and the amount of ink transfer.

There have also been studies both experiments and computations dedicated to the influence of viscoelasticity on gravure printing [38, 10, 39]. Ahn et al. [38] examined the influence of elasticity through numerical computations using Oldroyd-B model and observed significant differences in the velocity field and pressure distribution in the cavity between viscoelastic and Newtonian fluids. Sankaran and Rothstein [10] conducted experimental investigation using polyethylene oxide (PEO) fluids to study the impact of viscoelasticity, gravity and gravure cell design on the fluid transfer in gravure printing. Filament stabilization due to elasticity was found to enhance or worsen the fluid removal, depending on whether the fluid removal direction is aligned with or opposite to the direction of gravity. Computational studies later by Lee et al. [39] on the influence of viscoelasticity in gravure printing using FENE-P constitutive model were in excellent agreement with experiments [10]. Their computations were able to extend beyond the parameters of the experiments to investigate a larger viscoelastic parameter space.

In the current work, we investigated the impact of shear-thickening—namely the magnitude and critical shear rate for onset of shear-thickening—on liquid transfer from an idealized gravure cell. The model experimental setup for the gravure printing study was the same as those adopted by Sankaran and Rothstein 2012 [10]. The model fluids used in the study were shear-thickening fumed silica nanoparticle dispersions in polypropylene glycol. The shear and extensional rheology of this system has been well characterized in literature [40, 41]. The role of shear-thickening on the amount of liquid transfer from an idealized gravure cell was studied by conducting experiments on

nanoparticle dispersions at various particle concentrations. The experimental liquid transfer behavior was further examined by transient finite element computations using a generalized Newtonian fluid model.

2 Methods and Materials

2.1 Gravure experimental setup

In our experiments, a modified version of a filament stretching extensional rheometer was used to model the pickout process for an idealized gravure cell or cavity [10]. The experimental setup, shown in Figure 1, consists of a computer-controlled linear motor attached to a aluminum plate which is in-line with the cavity. The initially cylindrical fluid bridge was stretched vertically from the cavity with constant velocity. In real gravure processes, the fluid bridge experiences a combination of shear and extensional deformation, with the latter being dominant at later times near the mid-plane and the former being important at earlier times and near the end plate/cell. For simplicity, the touch down process that would occur in the real roll-to-roll coating is not modeled— instead the initial fluid bridge has a finite aspect ratio. A truncated cone shaped cavity was fabricated by casting PDMS (Silgard 184) onto a negative mold of the cavity machined into aluminum. The cavity has a sidewall angle of $\alpha = 75^\circ$ from horizontal, radius of $R = 2.5$ mm and a depth of $h = 1$ mm. The real gravure rollers have cavity features that are typically ten to hundred microns in order. Here the cavity dimensions were scaled for the convenience of a lab scale study. The effect of cavity size was probed numerically. A cylindrical fluid filament was held between the plate and cavity at an initial aspect ratio of $L_i/R = 0.3$, where L_i is the separation. The top plate was separated at different velocities ranging from 0.1 - 200 mm/s to a final aspect ratio of $L_f/R \sim 32$, up to which the filaments survived in only a few cases. The stretching speed corresponded roughly to printing speed. The inertia effects were negligible in these tests as the Reynolds numbers were all very low, $\mathrm{Re} < 5 \times 10^{-2}$. Reynolds number is the ratio of inertial to viscous forces given by, $\mathrm{Re} = D_0 U \rho/\eta_0$. Here $\mathrm{D_0}$ and U are the characteristic diameter and velocity, while ρ and η_0 are the fluid density and viscosity. Because gravity is significant at these dimensions (the initial Bond number is greater than one, $\mathrm{Bo} \sim 2$), tests were performed with cavity on both top and bottom configurations. Bond number quantifies the relative importance of gravity to interfacial tension forces and is given by, $\mathrm{Bo} = \rho g {D_0}^2/4\sigma$. Here σ is the interfacial tension of the fluid.

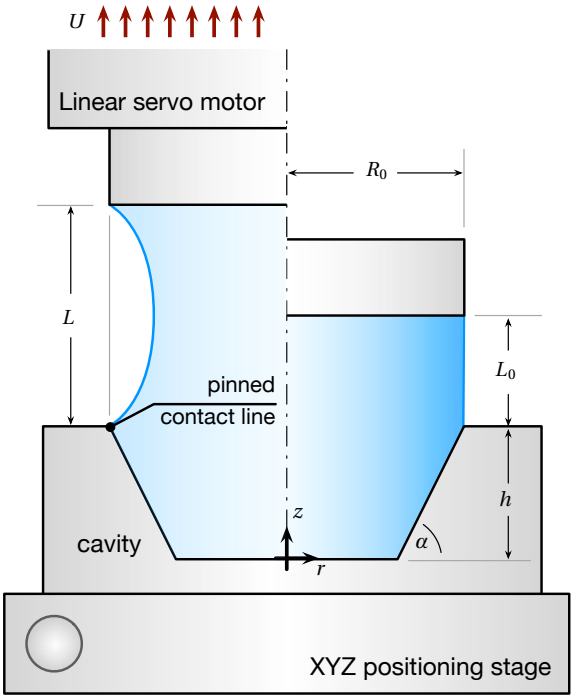

Figure 1: Schematic diagram of experimental setup used for idealized gravure cell study.

The filament profile evolution during the stretch and the breakup process was examined using a high-speed video camera (Vision Research, Phantom 4.6). The initial and final mass of the fluid in the cavity was measured using a high precision mass balance (Mettler AC 100). The pickout fraction is defined as, $\phi = m/M$, where m is mass transferred to the top plate and M is the total mass of the fluid. All the fluid transferred was assumed to be on the top plate; fluid lost by other mechanisms were ignored. The uncertainty in the experimentally measured values of pickout is just 2% or less.

2.2 Numerical method

Numerical modeling of the liquid transfer from an idealized gravure cell was carried out by solving the Navier-Stokes equations with a generalized Newtonian constitutive law. The equations were solved using the Galerkin finite element method (GFEM) with the adaptive step trapezoid rule for time marching. The transient free surface position and domain deformation were solved

using the ALE description. The complete set of governing equations is given below:

$$\mathbf{0} = \rho\left(\frac{\partial \mathbf{v}}{\partial t} + \mathbf{v}\cdot\nabla\mathbf{v}\right) - \nabla\cdot\mathbf{T} - \rho\mathbf{g} \tag{1}$$

$$0 = \nabla\cdot\mathbf{v} \tag{2}$$

$$\mathbf{0} = \nabla\cdot\tilde{\mathbf{D}}\cdot\nabla\boldsymbol{\xi}(\mathbf{x}) \tag{3}$$

with unknown fluid velocity $\mathbf{v}$, pressure p, and mesh positions $\mathbf{x}$. The fluid is incompressible with density ρ. The mesh equation was posed in terms of the inverse mapping of the mesh positions to a fixed logical coordinates $\boldsymbol{\xi}$. The parameter $\tilde{\mathbf{D}}$, which controls the mesh spacing, was set to the unit tensor.

The generalized Newtonian constitutive law for the fluid state of stress $\mathbf{T}$ is

$$\mathbf{T} = \eta(\dot{\gamma})2\mathbf{D} \tag{4}$$

i.e., the viscosity η is rate-dependent rather than constant. The scalar rate-of-strain metric is the usual $\dot{\gamma} = \sqrt{-2II_{2\mathbf{D}}}$ where $\mathbf{D}$ is the rate-of-strain tensor $2\mathbf{D} = (\nabla\mathbf{v} + \nabla\mathbf{v}^T)$ and $II_{\mathbf{A}}$ denotes the second invariant of a tensor $\mathbf{A}$. The details of our generalized Newtonian constitutive law are described with the shear rheometry results in Sec. 2.3. The free surface is governed by normal stress balance and kinematic boundary conditions

$$\mathbf{n}\cdot\mathbf{T} = (-p_{\text{amb}} + \kappa\sigma)\,\mathbf{n} \tag{5}$$

$$0 = \mathbf{n}\cdot(\mathbf{v} - \dot{\mathbf{x}}) \tag{6}$$

where $\mathbf{n}$ is the outward pointing boundary normal, κ denotes the boundary curvature, σ is the interfacial tension, and p_{amb} is the ambient pressure. The symmetry axis is governed by the shear-free condition, and the moving wall is governed by the explicit boundary conditions

$$0 = x_z - f(t) \tag{7}$$

$$0 = v_z - \dot{f}(t) \tag{8}$$

where $f(t)$ describes the axial position of the moving plate in time. From observations made using a high speed camera, the three-phase contact line appeared to be pinned at the corner of the gravure cell when in the cavity-on-bottom configuration. The contact-line motion was difficult to observe for the cavity-on-top configuration. The liquid was clearly drawn from within the gravure

cell, however, whether the fluid fully dewetted from the wall of the gravure cell or left behind a thin film could not be ascertained. In order to simplify the numerical simulations, our initial assumption was that the contact line remained pinned during the liquid transfer process. The pinned contact line assumption will be later revisited in section 3.1 when comparisons are made between the experimental and numerical results.

The typical domain was tessellated into a structured mesh of 12×640 (radial $\times$ axial) quadrilateral elements. Velocity and pressure were supported on Q_2P_{-1} elements [42] and mesh position was supported on Q_2. The final algebraic equations were solved with Newton's method using analytic Jacobian. Each Newton step was solved by LU decomposition using a frontal algorithm parallelized by OpenMP and executed on up to 12 processors in shared memory configuration.

2.3 Test fluids

Our model fluid was fumed silica nanoparticles (Aerosil @200, Evonik Industries; primary particle diameter 20 nm, specific surface area $200\,\mathrm{m}^2/\mathrm{g}$) dispersed in polypropylene glycol (Aldrich Chemicals, average M.W $1000\,\mathrm{g/mol}$). A series of test fluids with varying concentration (7.5 wt% to 20 wt%) were prepared by mixing in a blender for an hour until a transparent and colorless dispersion was obtained. The resulting dispersions were kept in the vacuum chamber for several hours to remove the air bubbles before use [41]. The surface tension was measured using a pendant drop tensiometer (Dataphysics OCA 15plus). The surface tension was found to be insensitive to the nanoparticle concentration, and was found to be $\sigma \approx 30\,\mathrm{mN/m}$. As described in the following sections, the shear and extensional rheology indicate that the test fluids are well-approximated as generalized Newtonian liquids.

Shear Rheology

The shear rheology was probed using a stress-controlled TA DHR-3 rheometer using a 40 mm aluminum parallel-plate geometry at a constant temperature of 25°C temperature with a solvent trap to prevent evaporation. The samples were pre-sheared to erase any shear history during sampling preparation and handing [43, 44]. After pre-shear, samples were allowed to rest for 4 minutes to reach equilibrium. Steady shear viscosity measurements were conducted in the shear rate range of $0.1\,\mathrm{s}^{-1} \leq \dot{\gamma} \leq 100\,\mathrm{s}^{-1}$.

As shown in Figure 2, the test fluids were all found to be shear thinning at low shear rates.

This behavior has been shown to result from the formation of strings of particles aligned along the direction of shear fields [45]. All four test fluids were found to shear-thicken beyond a critical shear rate. The magnitude of shear-thickening was found to progressively increase with increasing particle concentration from 7.5 wt% to 20 wt%. The mechanism for the shear-thickening behavior of these nanoparticles has been attributed to the formation of large hydrodynamic-induced clusters of nanoparticles [45]. The critical shear rate for the onset of shear rate of shear-thickening was found to decrease with increasing particle concentration. Beyond a second critical shear rate, the fluids are expected to shear-thin; although experimental limitations in this study prevented this observation at high concentration test fluids, previous studies have shown the shear-thinning behavior [46, 47, 41, 40].

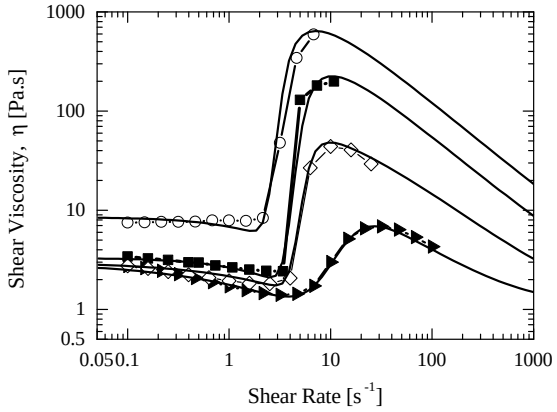

Figure 2: Steady shear viscosity as a function of shear rate for a series of fumed silica dispersions in PPG. The data include different particle concentrations of (▶) 7.5 wt%, (◇) 10 wt %, (■) 15 wt% and (◯) 20 wt%. Solid lines are fits of the high-rate-thinning model of Equation (9) to experimental steady shear rheology data for various particle concentrations.

A generalized Newtonian constitutive model

The steady-shear rheology data for all particle concentrations were fit by a generalized Newtonian fluid model. The shear-thickening behavior of Aerosil/PPG systems is well-documented, and piece-wise generalized Newtonian constitutive laws to describe the shear viscosity have been previously reported [40, 47]. To simplify the piece-wise description, we formulate a new generalized

Newtonian constitutive law

$$\eta_t(\dot{\gamma}) = \left\{ \frac{\eta_\infty}{A} + \left(\eta_0 - \frac{\eta_\infty}{A}\right) \left[1 + (\lambda_1 \dot{\gamma})^{B_1}\right]^{\frac{n_1-1}{B_1}} \right\} \left\{ 1 + A - A \left[1 + (\lambda_2 \dot{\gamma})^{B_2}\right]^{\frac{n_2-1}{B_2}} \right\} \tag{9}$$

The zero-shear and infinite-shear viscosities are η_0 and η_∞, and the extent of shear-thickening is determined by A. The model is essentially a product of two Carreau models, one each for the shear-thinning and shear-thickening regions denoted by the subscripts 1 and 2, respectively. Each part of the model has a time constant λ, the power law exponent n, and a dimensionless transition parameter B. The critical shear rates for thinning and thickening are thus $1/\lambda_1$ and $1/\lambda_2$, respectively. For each suspension concentration, the parameters were fit to the measured steady shear viscosity and the results superimposed over the data in Figure 2. The values of the generalized Newtonian constitutive law parameters used to fit each of the fluids in Figure 2 are presented in Table 1.

Extensional Rheology

Extensional rheology was probed by filament stretching extensional rheometry (FiSER), which is typically used to characterize fluids with a shear viscosity $\eta > 1\,\mathrm{Pa\,s}$ [48, 49, 50, 51]. We use the FiSER type II test, where the top plate is separated from the bottom plate with exponential velocity profile to impose a nearly constant extension rate $\dot{\varepsilon}$ on the fluid filament at the mid-plane. The apparent extension rate $\dot{\varepsilon}_{\mathrm{app}}$ is calculated from the mid-filament diameter decay rate, and used to infer the apparent extensional viscosity $\eta_E = \langle \tau_{zz} - \tau_{rr} \rangle / \dot{\varepsilon}_{\mathrm{app}}$, where the elastic normal stress difference $\langle \tau_{zz} - \tau_{rr} \rangle$ is estimated from force measurement at the top plate and an approximate mid-plane force balance [52, 49].

In Figure 3, the extensional viscosity is shown with respect to Hencky strain for test fluids with concentrations > 10 wt%. Unfortunately, measurements were not possible for concentrations below 10 wt% because of limitations of the force transducer sensitivity. As previously reported [41, 53, 54], the extensional thickening of the test fluids was found to increase with increasing nanoparticle concentration. Without adjusting any of the model parameters, the generalized Newtonian constitutive model qualitatively predicts the extensional rheology of the test fluids in Figure 3. The agreement, however, is not perfect. The experimentally measured maximum extensional viscosities are systematically larger than the values predicted by the generalized Newtonian model. This discrepancy has also been described in [41], where analysis of extensional viscosity based on a modified Trouton

ratio using the corresponding shear rate

$$\mathrm{Tr} = \frac{\eta_E}{\eta(\dot{\gamma})} = \frac{\eta_E}{\eta(\sqrt{3}\dot{\varepsilon})} \tag{10}$$

demonstrated that extensional thickening is more dramatic than predicted by shear-thickening alone, and occurs at a slightly lower critical extension rates than the expected value of $\dot{\gamma}_c/\sqrt{3}$, where $\dot{\gamma}_c$ is the critical shear rate for the onset of shear thickening. These effects are exacerbated with increasing particle concentration. For our test fluids, the particle concentrations were low enough that the generalized Newtonian model appears well-justified.

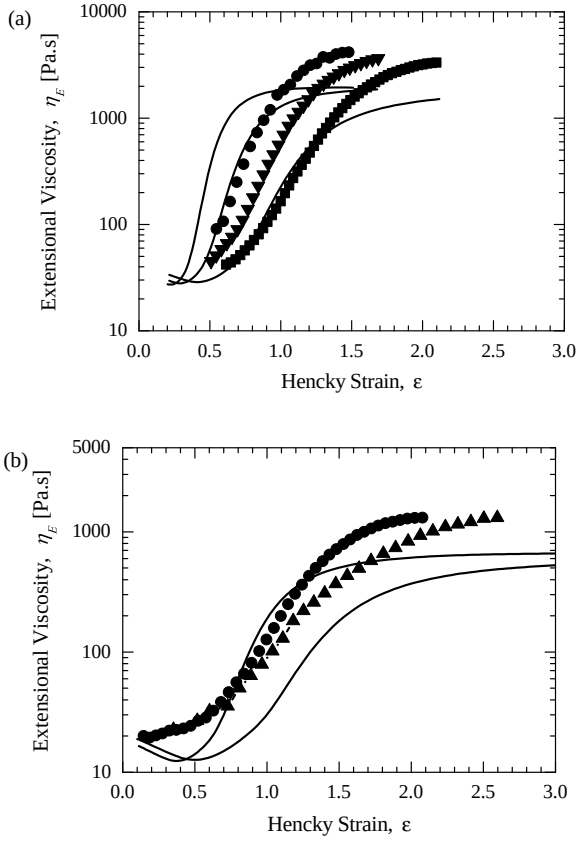

Figure 3: Experimental (symbols) and simulated (lines) FiSER type II extensional rheology data for different concentrations of silica nanoparticles dispersed in PPG. The concentrations include a) 20 wt% and b) 15 wt%. The imposed extension rates are (■) 3 s^{-1}, (▲) 4 s^{-1} and (●) 5 s^{-1}.

For both 15 and 20 wt% test fluids, beyond extension rates of $\dot{\varepsilon} > 6$ s^{-1}, the extensional behavior could not be characterized using FiSER due to the formation of conical shaped filament profiles that made calculation of the extension rate and extensional viscosity impossible. These

flow transitions will be discussed in more detailed in the context of liquid transfer measurements in section 3.

3 Results and discussion

Measurements of liquid transfer from an idealized gravure cell were conducted on a series of nanoparticle dispersions. Pickout fractions were measured as a function of increasing stretching velocity from 0.1 to 200 mm/s. The liquid filament profile evolution of the 15 wt% test fluid was captured by video analysis and presented in Figures 4 and 5. For comparison, the predictions of the numerical simulations are presented alongside the experiments in Figure 4. The results show excellent agreement between the measured and simulated shapes and shape transitions.

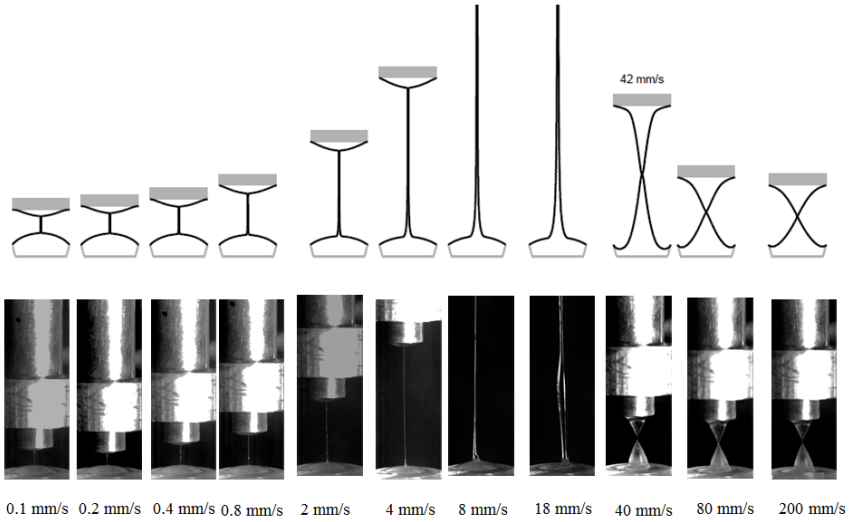

Figure 4: Terminal filament interface profiles for the 15 wt% silica nanoparticle dispersion in PPG with cavity-on-bottom. Top: computational results for comparison.

The pickout behavior of shear-thickening 15 wt% silica dispersion is shown in Figure 6 for both cavity on top and bottom cases. Pickout at vanishing velocities is higher for the cavity-on-top configuration than for the cavity-on-bottom configuration; in this vanishing capillary number ($\mathrm{Ca} = \eta U/\sigma$) regime, the pickout is a quasi-equilibrium process governed solely by surface tension and gravity, implying that pickout is gravity-enhanced in the cavity-on-top configuration and vice-versa due to gravitational sagging of the quasi-equilibrium liquid bridge profile [10, 39].

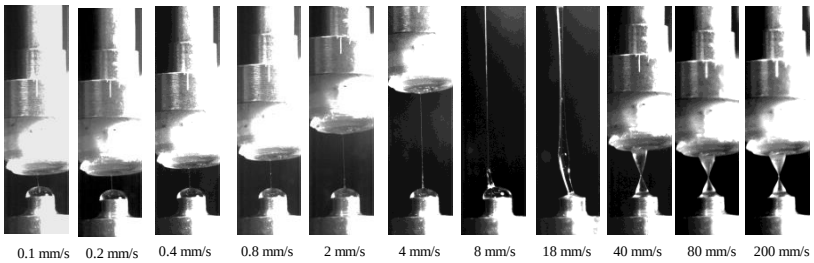

Figure 5: Terminal filament interface profiles for the 15 wt% silica nanoparticle dispersion in PPG with cavity-on-top.

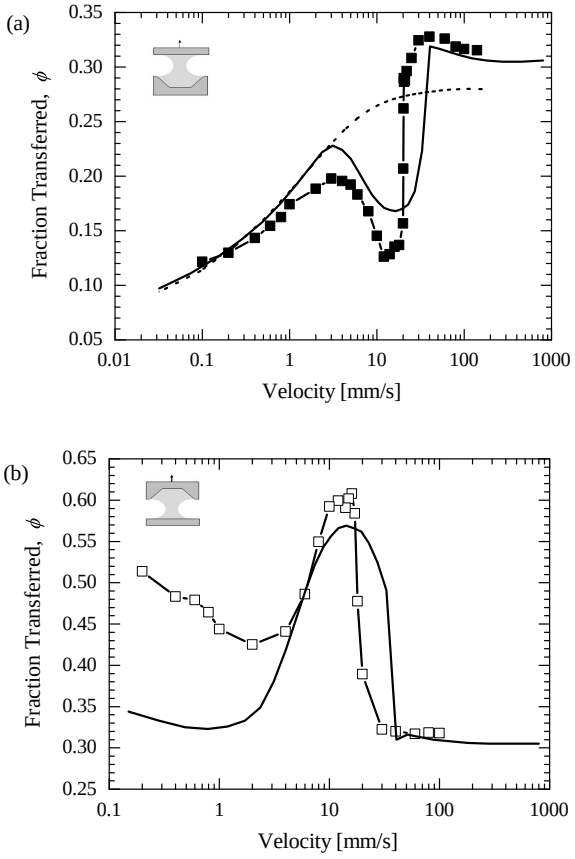

Figure 6: Experimental (symbols) and computed (solid lines) fraction of fluid transferred from the cavity as a function of velocity for a 15 wt% fumed silica nanoparticle dispersion in PPG for two different cavity configurations. a) Cavity on bottom b) Cavity on top. (dotted line) Pickout fraction computed for Newtonian fluid with viscosity of 3.3 Pa s for cavity on bottom case is also shown in Figure a.

At low velocities, $0.1 < U < 2\,\text{mm/s}$, with moderate Ca, the strain rates are low enough that the shear-thickening and extensional hardening are not active. The pickout behavior in this regime is qualitatively similar to that of Newtonian fluid, computed for comparison and shown as a dashed line in Figure 6a. This is consistent with reports in literature [10, 39]. One important observations from Figure 6b is that even in this Newtonian regime, the absolute value of pickout is severely under-predicted by computations. We will discuss in section 3.1 the possible role that contact line and liquid de-wetting can play in resolving this discrepancy.

At intermediate velocities, $2 < U < 18\,\text{mm/s}$, the pickout is dramatically depressed for the cavity-on-bottom configuration and dramatically enhanced for the cavity-on-top configuration. Both Figure 4 and Figure 5 show that, within this regime, with increasing velocity a more elongated filaments with increasing life time persist due to viscous stabilization by extensional-thickening which resists capillary break-up. The extensional thickening of the fluid allows more fluid to be removed from the cavity by increasing the break-up time of the fluid filament. A similar behavior was also reported for viscoelastic fluids, where long-lived filaments, that evolve as a result of thickening of the fluid's extensional viscosity, result in gravitational drainage over longer process time and dramatically influence the final pickout [10, 39]. The model computations correctly predict the pickout behavior, specifically the critical velocities at which the local extrema in pickout occur.

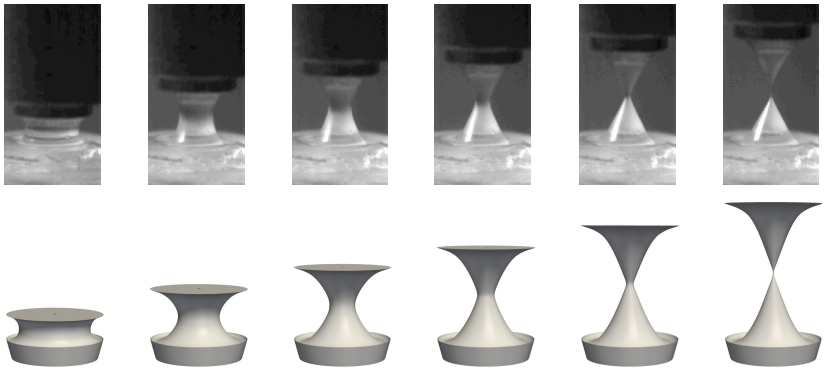

Figure 7: Comparison of the evolution of conical filament profile at $U = 100\,\text{mm/s}$ between experiment and computation for the 15 wt% silica in PPG dispersion.

At high velocities, $U > 18\,\text{mm/s}$, the pickout fraction begins to increase again and plateaus beyond 50 mm/s. The filaments profile beyond 50 mm/s evolve not as cylindrical but as conical profiles as shown in Figure 4. The profile evolutions with time/strain observed in the experiments

and predicted by the computations are shown in Figure 7. They change very little with increasing velocity beyond a critical velocity of about 50 mm/s. This phenomenon is what prevented FiSER tests at high extension rate, as described earlier. As illustrated in Figure 8, this conical profile evolution is a result of self-accelerating shear-thinning at the mid-plane, where the strain-rate is highest and large enough to deform the fluid at rates well past the shear thickening regime into the second, more severe shear thinning regime observed in Figure 2. This resembles the phenomenon reported for yield stress fluids in extensional flows [55, 56]. Removing the thinning of the shear and extensional viscosity at the highest deformation rates in the generalized Newtonian constitutive model was found to suppress the formulation of the conical filament profiles. In the velocity range, $18 < U < 50$ mm/s, the recovery of the fluid pickout from a minimum value represents a transition in pickout which corresponds to a shift in the dominant fluid behavior from extensional thickening to shear-thinning.

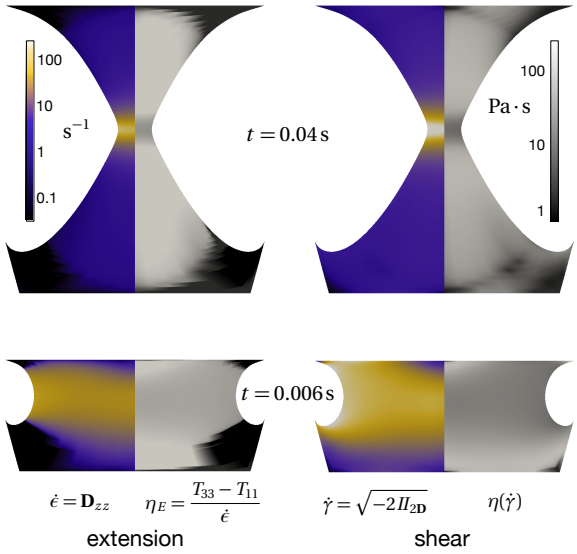

Figure 8: Contour plots of viscosity and the corresponding strain rates, during conical profile evolution computed at $U = 100$ mm/s for the 15 wt% silica nanoparticle model fluid

So far, we have described qualitatively the correspondence between pickout features with respect to velocity. The description of strain-rate of the pickout process to quantitatively correlate rheology features is not simple, as the flow is a combination of shear and extensional. Based on the discussion in [39] of the relevant strain rate governing pickout fraction, we posit that that a sensible way to convert the stretching velocity into a process strain rate is by using the "initial shear" rate U/R_0,

rather than the initial extension rate U/L_0, which may be more intuitive at first. To illustrate, Figure 9 shows computed pick-out results for the model generalized Newtonian fluid, varying initial liquid bridge radius R_0 and height L_0 (aspect ratio $\Lambda_0 = R_0/L_0$). The pickout fraction is scaled with the process strain rate defined as $\dot{\gamma} = U/R_0\Lambda_0^{-1/3}$, where $\Lambda_0^{-1/3}$ is an empirical dimensionless correction factor. The local extrema in pickout fraction align very well, implying that $\dot{\gamma}$ is indeed the appropriate measure for the process strain rate.

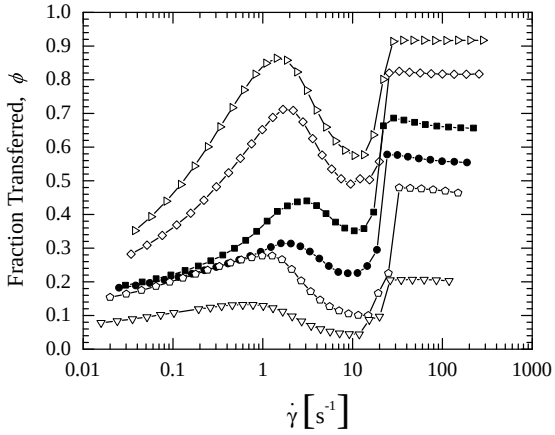

Figure 9: Pickout data scaled against strain-rate defined as, $\dot{\gamma} = U/R_0{\Lambda_0}^{-1/3}$. The data include for several aspect ratios Λ_0 of (▷) 0.15, (◇) 0.20 at L_0 = 0.75 mm; (■) 0.31, (●) 0.51 at R_0 = 0.75 mm and (⬠) 1.00, (▽) 2.00 at R_0 = 5.00 mm.

The influence of rheological features on pickout was further explored by experiments at different particle concentrations ranging from $7.5 - 20$ wt%. The experiments and computations of the pickout behavior with increasing velocity, for the case where the cavity is on the bottom, are shown in Figure 10a and b respectively. With increasing particle concentration, the critical shear rates for shear-thickening and shear-thinning was found to shift to lower shear rates as shown in Figure 2. Correspondingly, the local extrema in the pickout fraction shift to lower process strain rates, again matching the critical shear rates for the rheological features. The extent of shear-thickening increases with particle concentrations, and the local minimum pickout is correspondingly deeper in the stabilized filament regime. The experiments and computations of the pickout behavior, for the case of cavity on top, is also presented in Figure 11a and b respectively. The height and position of the local maximum pickout correspond well to the critical shear rate and extent of shear-thickening. A more dramatic illustration is given in Figure 12 and Figure 13, where pickout

is computed for model liquids with a much wider variation in critical shear rates and extents of shear-thickening that can be produced experimentally.

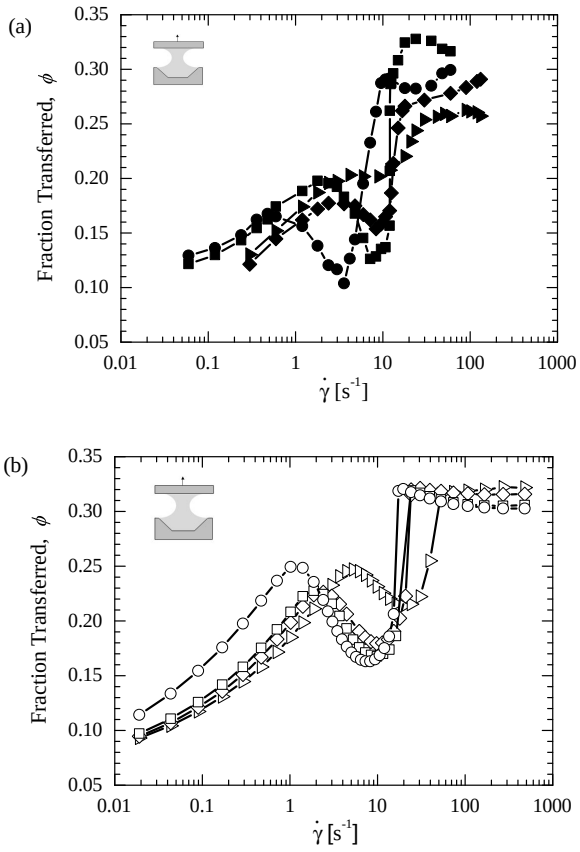

Figure 10: a) Experimental (filled symbols) and b) computed (hollow symbols) pickout fraction for a series of concentrations of fumed silica nanoparticles dispersed in PPG for cavity on the bottom configuration. The data include particle concentrations of (►) 7.5 wt%, (♦) 10 wt%, (■) 15 wt% and (●) 20 wt%.

3.1 Effect of moving contact line

The generalized Newtonian model for fumed silica dispersions captures qualitatively the pick-out behavior with respect to stretching velocity, as demonstrated in Figure 6 for the 15 wt% dispersion. The computations are expected to be in best agreement with experiment at low stretching velocities where strain rates remain low enough for the liquid to be nearly Newtonian. This appears to be the case for the cavity-on-bottom configuration in Figure 6a. However, the results for the cavity-on-top configuration deviate significantly in the low stretching velocity regime Figure 6b.

Moreover, our previous studies focused on quantitatively matching experimental and computa-

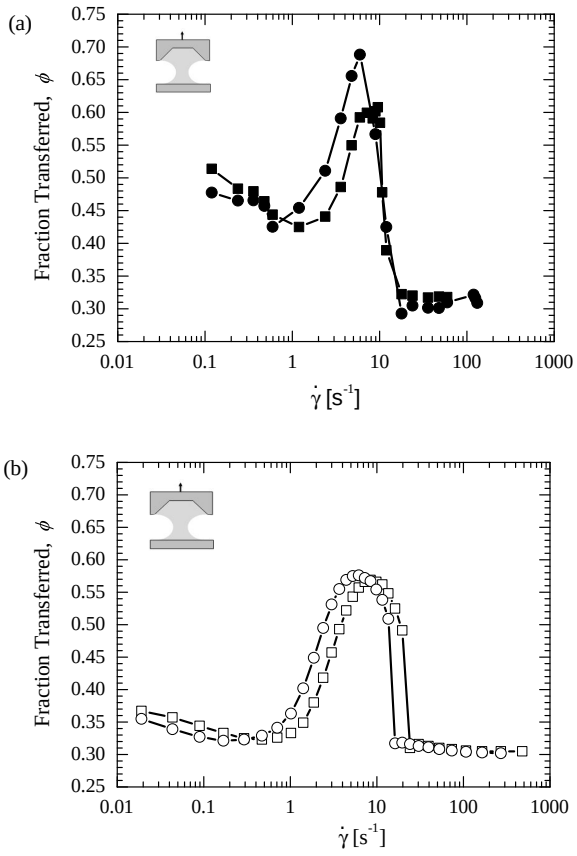

Figure 11: a) Experimental (filled symbols) and b) computed (hollow symbols) pickout fraction for a series of concentrations of fumed silica nanoparticles dispersed in PPG for the cavity on the top configuration. The data include particle concentrations of (■) 15 wt% and (●) 20 wt%.

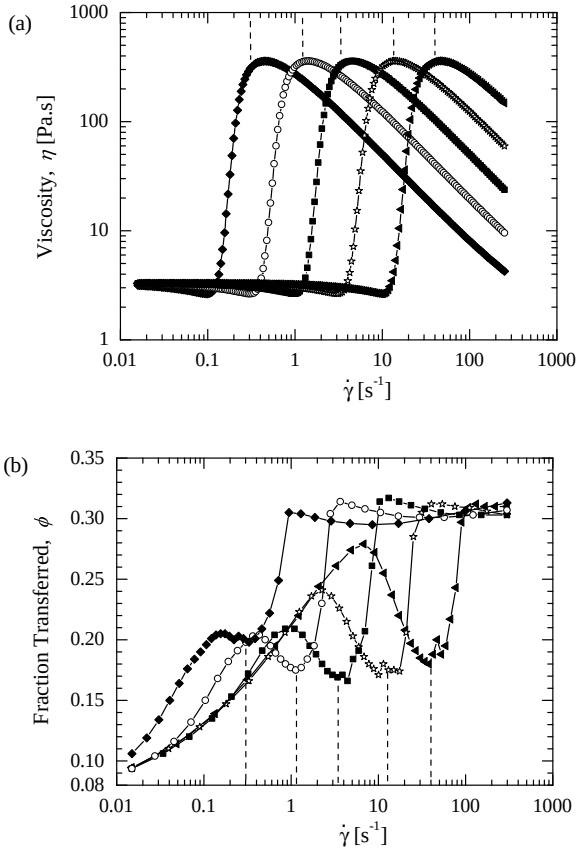

Figure 12: Computations of a) shear rheology given in Equation 9 with varying model parameter, λ_2, inverse of critical shear-rate for the onset of shear-thickening and b) the corresponding pickout fraction. The data include varied parameter λ_2 values of (♦) 5 , (◯) 1.6, (■) 0.5, (⋆) 0.16 and (◄) 0.05 s.

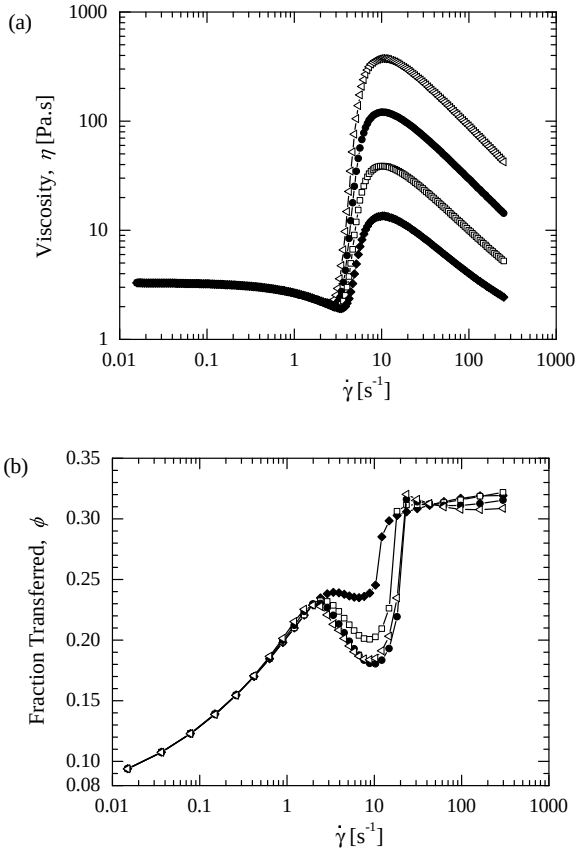

Figure 13: Computations of a) shear rheology given in Equation 9 with varying model parameter, A, amplitude of shear-thickening and the corresponding b) pickout fraction. The data include varied parameter A values of (⧫) 160, (□) 500, (●) 1600 and (◁) 5000 Pa s.

tional pick-out results only for the cavity-on-bottom configuration [10, 39], and noted only qualitative agreement for the cavity-on-top configuration. For the current study, computed predictions for the cavity-on-top configuration match better at high stretching velocities where non-Newtonian behavior is stronger. To explain this discrepancy, we revisit the pinned contact line assumption used in all computations described up to this point.

The pinned contact line assumption greatly simplifies modeling the liquid transfer experiment, but it cannot describe the de-wetting of liquid from the cavity wall. In experiments, this assumption was justified by direct observation whenever the cavity was held stationary in the cavity-on-bottom configuration. In a previous study, high pick-out fractions for viscoelastic liquid in the inverted configuration suggested that liquid was being transferred additionally by de-wetting from the cavity wall, though direct observation was not possible due to experimental challenges [10].

In the low stretching velocity regime where the liquid is nearly Newtonian, pinned contact line is the leading order assumption in our computational model. Thus, we hypothesize that the difference in computed and experimentally determined pick-out for inverted experiments at low stretching velocity is due to significant de-wetting. To test this hypothesis, we modeled de-wetting within our finite element framework based on the Navier slip law following the formulation in [57]. We further simplified the dynamic contact line modeling of [57] by introducing an ad hoc relationship between contact angle and dimensionless wetting/de-wetting velocity, capillary number Ca

$$\theta = \theta_{\text{rec}} + \frac{\theta_{\text{adv}} - \theta_{\text{rec}}}{\left(1 + \frac{v}{B}\mathrm{e}^{k\text{Ca}}\right)^{1/v}} \tag{11}$$

where

$$B = \frac{\theta_{\text{eq}} - \theta_{\text{rec}}}{\theta_{\text{adv}} - \theta_{\text{rec}}} \tag{12}$$

and v is chosen such that

$$0 = B - \frac{1}{(1 + v/B)^{1/v}} \tag{13}$$

to ensure $\theta = \theta_{\text{eq}}$ when $\text{Ca} = 0$. This relationship is not rooted in any hydrodynamic or molecular kinetic theory (see, e.g. [58, 59, 60]), but rather describes phenomenologically the behavior of apparent dynamic contact angle with respect to wetting velocity. This simple relation is advantageous over physically derived models because it gives sensible values over all $-\infty < \text{Ca} < \infty$ and has a continuous derivative. Other models such as Tanner's law require piece-wise description for wetting and de-wetting cases, as well as matching at $\text{Ca} = 0$.

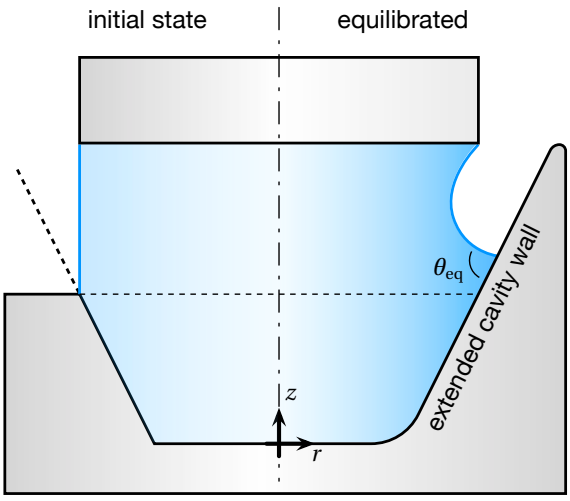

Figure 14: Modified geometry to allow easier modeling of the unpinned contact line.

Equation (11) is parameterized to set an effective equilibrium contact angle, asymptotic values of maximum and minimum advancing and receding contact angles (allowing for asymmetricity about the equilibrium contact angles is observed in real systems with moderate Ca [58]), and sensitivity of the contact angle to contact line velocity. In Figure 15, large values of the sensitivity parameter k indicate that the contact angle is a strong function of contact line velocity and that the contact line is relatively immobile (pinned), whereas small values of k indicate that the contact angle is nearly static and the contact line is more mobile.

To ensure that the mobile contact line never encounters the top corner of the cavity, we modified the cavity geometry as shown in Figure 14 such that the cavity wall extends farther up; this allows relatively coarse radial mesh resolution to sufficiently capture the solid wall boundary for accurate representation of contact angles. The total liquid volume is kept constant at 30 microliters, which is close to the pinned contact line case of 32 microliters. The initial liquid bridge is no longer a true cylinder, but instead the equilibrium configuration of a liquid bridge that makes the equilibrium contact angle with the cavity wall; it is achieved by starting from a cylindrical configuration and carrying out the transient computations until it achieves the steady or equilibrium state. For comparison, the pinned contact line model computations were executed from the same initial condition, with the contact line re-pinned before stretching computations.

Based on experimental observation, the equilibrium contact angle between 15 wt% Si-PPG suspension and a flat PDMS substrate is close to $\theta_{eq} = 70^{\circ}$. For lack of physical data, we set the

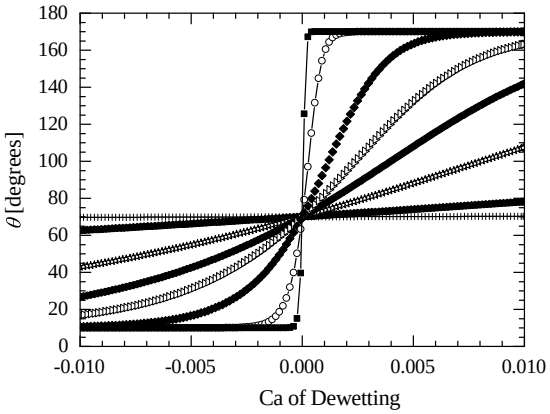

Figure 15: Contact angle model evaluated for fixed $\theta_{\rm eq}$, $\theta_{\rm adv}$, and $\theta_{\rm rec}$ for various values of k. The data include k values of, (+) 1.00×10^1, (⬠) 2.80×10^1, (⋆) 1.21×10^2, (◀) 2.450×10^2, (▷) 4.08×10^2, (⧫) 8.26×10^2, (●) 3.54×10^3 and (■) 2.00×10^4.

maximum and minimum dynamic contact angle values to be $\theta_{\rm adv} = 170^\circ$ and $\theta_{\rm rec} = 10^\circ$, i.e. $\pm 10^\circ$ from the geometrical limits. A preliminary study to choose a reasonable value of k was carried out by fixing the stretching velocity to $U = 0.2$ mm/s where the pick-out results between experiments and the computation were most different, the results presented in Figure 16 reveal that pickout generally increased as the value of k was decreased (the contact line was less pinned and contact angle more static).

Choosing a value of k where the contact line is unpinned in a regime where pickout results are insensitive to its value ($k \approx 10$) fully specifies—together with the above parameters $\theta_{\rm eq}$, $\theta_{\rm adv}$, and $\theta_{\rm rec}$—the contact angle model in Eqs. (11)–(13). We use these parameters to compute pickout fraction over a range of stretching velocities for comparison with the data, as shown in Figure 17. The modified model with unpinned contact line qualitatively reproduces the experimentally observed pickout fraction at low stretching velocities in the gravity-assisted case, while having little effect on the gravity-adverse cases. While the current contact line modeling may need some further refinement, the predicted trends do support the hypothesis that gravity-assisted pickout is amplified by de-wetting in the low stretching velocity regime.

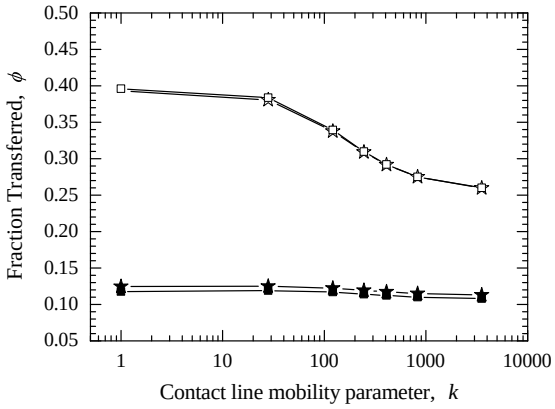

Figure 16: Comparison of pickout fraction with respect to k for a ($\star$) Newtonian fluid of viscosity 3.3 Pa s and (■) 15 wt% Si-PPG for fixed stretching velocity $U = 0.2\,\mathrm{mm/s}$, $\theta_{\mathrm{eq}} = 70^{\circ}$, $\theta_{\mathrm{adv}} = 180^{\circ}$, θ. The filled and hollow symbols correspond to cavity on bottom and top cases respectively.

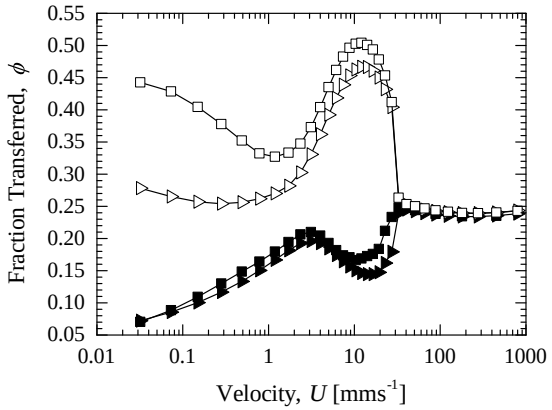

Figure 17: Comparison of pickout fraction of 15wt% Si-PPG with respect to stretching velocity at fixed $k = 10$ for (■) low k or mobile contact line and (►) high k or nearly pinned cases. The filled and hollow symbols correspond to cavity on bottom and top cases respectively.

4 Conclusions

In this paper, we investigated the impact of shear-thickening on liquid transfer from an idealized gravure cell through a combination of experiments and finite element computations. The amount of ink transfer with increasing velocity was measured for the shear-thickening dispersions at various particle concentrations. At low velocities, where the process strain rates are below the critical shear rate for shear-thickening, the pickout behavior is qualitatively similar to that of Newtonian fluids. At moderate velocities, the pickout exhibits a local extremum associated with persistence of long stable filaments due to extensional-thickening; the pickout is maximal when assisted by gravitational drainage (cavity-on-top) and vice versa. At high velocities, the filaments evolve into conical shapes due to shear-thinning. In this regime, the pickout is insensitive to velocity variation and is also unaffected by gravity. Computations predicted well the final pickout results when using a generalized Newtonian fluid model fitted to the measured shear viscosities. A systematic study of the impact of shear-thickening model parameters on pickout features corroborates the experimental observations. To correlate pickout behavior to rheology, the appropriate process strain rate appears to be an early time shear rate. The discrepancy between experimentally determined and computationally predicted pickout fraction in the low velocity regime was investigated by incorporating a de-wetting model. Introducing de-wetting through a simple contact angle model improves the matching of computed predictions to experimental results in this regime. This suggests that de-wetting plays a larger role when coupled with gravitational forces. In conclusion, we demonstrate a sound basis for optimizing the liquid transfer fraction during a gravure printing process, namely to ensure coating speeds that avoid certain regimes in the shear-viscosity function where a) rate-thickening induces viscous stabilization and b) rate-thinning induces yield-like behavior resulting in a high fraction of liquid stuck in the cavity.

5 Acknowledgments

The authors would like to thank NSF NSEC under Grant Nos. CMMI-1025020 and through NSEC under Grant Nos. CMMI-0531171, CMMI-1025020, and CMMI-1031171. Computations were supported in part by the Data Analysis and Visualization Cyberinfrastructure funded by NSF under Grant OCI-0959097; by NIH award NCRR S10RR02950 and an IBM Shared University Research (SUR) Award in partnership with CISCO, Qlogic and Adaptive Computing; and by

the Shared University Grid at Rice funded by NSF under Grant EIA-0216467, and a partnership between Rice University, Sun Microsystems, and Sigma Solutions, Inc.

Table 1: The fitting parameters of shear-thickening fluid model given in Equation (9) for several silica nanoparticle concentrations.

Silica [Wt %]	μ_o [Pa s]	μ_∞ [Pa s]	B_1	n_1	λ_1 [s]	B_2	n_2	λ_2 [s]	A
7.5	3.0	1.0	0.5	0.01	100	3.3	-2	62	16
10	3.0	1.0	0.6	0.11	100	10.0	-3	180	48
15	3.3	1.0	1.0	0.15	300	11.0	-0.9	200	300
20	8.5	1.0	1.0	0.15	300	11.0	-0.9	300	260

References

[1] R. R. Søndergaard, M. Hösel, F. C. Krebs, Roll-to-roll fabrication of large area functional organic materials, J. Polym. Sci. Part B: Polymer Physics 51 (1) (2013) 16–34.

[2] A. Hübler, B. Trnovec, T. Zillger, M. Ali, N. Wetzold, M. Mingebach, A. Wagenpfahl, C. Deibel, V. Dyakonov, Printed paper photovoltaic cells, Adv. Energy Mater. 1 (6) (2011) 1018–1022.

[3] W. Yue, T. T. Larsen-Olsen, X. Hu, M. Shi, H. Chen, M. Hinge, P. Fojan, F. C. Krebs, D. Yu, Synthesis and photovoltaic properties from inverted geometry cells and roll-to-roll coated large area cells from dithienopyrrole-based donor-acceptor polymers, J. Mater. Chem. A 1 (2013) 1785–1793.

[4] F. C. Krebs, T. Tromholt, M. Jørgensen, Upscaling of polymer solar cell fabrication using full roll-to-roll processing, Nanoscale 2 (2010) 873–886.

[5] M. Hösel, F. C. Krebs, Large-scale roll-to-roll photonic sintering of flexo printed silver nanoparticle electrodes, J. Mater. Chem. 22 (2012) 15683–15688.

[6] L. Gonzalez-Macia, A. Morrin, M. R. Smyth, A. J. Killard, Advanced printing and deposition methodologies for the fabrication of biosensors and biodevices, Analyst 135 (2010) 845–867.

[7] C. F. Huebner, J. B. Carroll, D. D. Evanoff, Y. Ying, B. J. Stevenson, J. R. Lawrence, J. M. Houchins, A. L. Foguth, J. Sperry, S. H. Foulger, Electroluminescent colloidal inks for flexographic roll-to-roll printing, J. Mater. Chem. 18 (2008) 4942–4948.

[8] A. M. Almanza-Workman, C. P. Taussig, A. H. Jeans, R. L. Cobene, Fabrication of three-dimensional imprint lithography templates by colloidal dispersions, J. Mater. Chem. 21 (2011) 14185–14192.

[9] G. Hernandez-Sosa, N. Bornemann, I. Ringle, M. Agari, E. Dörsam, N. Mechau, U. Lemmer, Rheological and drying considerations for uniformly gravure-printed layers: Towards large-area flexible organic light-emitting diodes, Adv. Funct. Mater. 23 (2013) 3164.

[10] A. K. Sankaran, J. P. Rothstein, Effect of viscoelasticity on liquid transfer during gravure printing, J. Non-Newtonian Fluid Mech. 175 - 176 (2012) 64 – 75.

[11] H. Kang, R. Kitsomboonloha, J. Jang, V. Subramanian, High-performance printed transistors realized using femtoliter gravure-printed sub-10 μm metallic nanoparticle patterns and highly uniform polymer dielectric and semiconductor layers, Adv. Mater. 24 (22) (2012) 3065–3069.

[12] M. M. Voigt, A. Guite, D.-Y. Chung, R. U. A. Khan, A. J. Campbell, D. D. C. Bradley, F. Meng, J. H. G. Steinke, S. Tierney, I. McCulloch, H. Penxten, L. Lutsen, O. Douheret, J. Manca, U. Brokmann, K. Sönnichsen, D. Hülsenberg, W. Bock, C. Barron, N. Blanckaert, S. Springer, J. Grupp, A. Mosley, Polymer field-effect transistors fabricated by the sequential gravure printing of polythiophene, two insulator layers, and a metal ink gate, Adv. Funct. Mater. 20 (2) (2010) 239–246.

[13] D. M. Campana, M. S. Carvalho, Liquid transfer from single cavities to rotating rolls, Journal of Fluid Mechanics 747 (2014) 545–571.

[14] S. Kumar, Liquid transfer in printing processes: Liquid bridges with moving contact lines, Annual Review of Fluid Mechanics 47 (1) (2015) 67–94.

[15] M. Pudas, S. Leppavuori, J. Hagberg, The absorption ink transfer mechanism of gravure offset printing for electronic circuitry, in: IEEE Transactions on Electronics Packaging Manufacturing, Vol. 25, 2002, pp. 335 – 343.

[16] B. Qian, K. S. Breuer, The motion, stability and breakup of a stretching liquid bridge with a receding contact line, J. Fluid Mech. 666 (2011) 554–572.

[17] D. Rivas, J. Meseguer, One-dimensional self-similar solution of the dynamics of axisymmetric slender liquid bridges, J. Fluid Mech. 138 (1984) 417–429.

[18] S. Gaudet, G. H. McKinley, H. A. Stone, Extensional deformation of Newtonian liquid bridges, Phys. Fluids 8 (10) (1996) 2568–2579.

[19] R. Gillette, D. Dyson, Stability of fluid interfaces of revolution between equal solid circular plates, Chem. Eng. J. 2 (1) (1971) 44 – 54.

[20] J. Meseguer, The breaking of axisymmetric slender liquid bridges, J. Fluid Mech. 130 (1983) 123–151.

[21] L. Rayleigh, On the instability of jets, Proc. London Math. Soc. 10 (1878) 4 – 13.

[22] J. A. F. Plateau, Experimental and theoretical researches on the figures of equilibrium of a liquid mass withdrawn from the action of gravity, Annual Report of the Board of Regents and Smithsonian Institution, Washington, DC (1863) 2568–2579.

[23] H. W. Kang, H. J. Sung, T.-M. Lee, D.-S. Kim, C.-J. Kim, Liquid transfer between two separating plates for micro-gravure-offset printing, J. Micromech. Microeng. 19 (2009) 015025.

[24] P. P. Bhat, O. A. Basaran, M. Pasquali, Dynamics of viscoelastic liquid filaments: Low capillary number flows, J. Non-Newton. Fluid Mech. 150 (2–3) (2008) 211 – 225.

[25] P. P. Bhat, S. Appathurai, M. T. Harris, M. Pasquali, G. H. McKinley, O. A. Basaran, Formation of beads-on-a-string structures during break-up of viscoelastic filaments, Nature Physics 6 (8) (2010) 625–631.

[26] C. Powell, M. Savage, J. Guthrie, Computational simulation of the printing of newtonian liquid from a trapezoidal cavity, Int. J. Numer. Methods Heat Fluid Flow 12 (2002) 338–355.

[27] S. Dodds, M. da Silveira Carvalho, S. Kumar, Stretching and slipping of liquid bridges near plates and cavities, Phys. Fluids 20 (2009) 092103.

[28] S. Dodds, M. da Silveira Carvalho, S. Kumar, Stretching liquid bridges with moving contact lines: The role of inertia, Phys. Fluids 23 (2011) 092101.

[29] W.-X. Huang, S.-H. Lee, H. J. Sung, T.-M. Lee, D.-S. Kim, Simulation of liquid transfer between separating walls for modeling micro-gravure-offset printing, Int. J. Heat and Fluid Flow 29 (5) (2008) 1436–1446.

[30] X. Yin, S. Kumar, Flow visualization of the liquid-emptying process in scaled-up gravure grooves and cells, Chem. Eng. Sci. 61 (2006) 1146–1156.

[31] X. Yin, S. Kumar, Lubrication flow between a cavity and a flexible wall, Phys. Fluids 17 (2005) 063101.

[32] C. Powell, M. Savage, P. Gaskell, Modelling the meniscus evacuation problem in direct gravure coating, Chemical Engineering Research and Design 78 (1) (2000) 61 – 67.

[33] N. Hoda, S. Kumar, Boundary integral simulations of liquid emptying from a model gravure cell, Phys. Fluids 20 (2008) 092106.

[34] S. Dodds, M. S. Carvalho, S. Kumar, The dynamics of three-dimensional liquid bridges with pinned and moving contact lines, J. Fluid Mech. 707 (2012) 521–540.

[35] M. A. Johnson, Viscoelastic roll coating flows., Ph.D. thesis, University of Maine (2003).

[36] D. H. Ahmed, H. J. Sung, D.-S. Kim, Simulation of non-newtonian ink transfer between two separating plates for gravure-offset printing, Int. J. Heat and Fluid Flow 32 (2011) 298–307.

[37] F. Ghadiri, D. H. Ahmed, H. J. Sung, E. Shirani, Non-newtonian ink transfer in gravure-offset printing, Int. J. Heat and Fluid Flow 32 (2011) 308–317.

[38] S. Ahn, S. Lee, Y. Na, Elasticity effect on the ink transfer process in gravure printing, in: Computational Science and its Applications, 2008, pp. 565–575.

[39] J. A. Lee, J. P. Rothstein, M. Pasquali, Computational study of viscoelastic effects on liquid transfer during gravure printing, J. Non-Newtonian Fluid Mech. 199 (2013) 1 – 11.

[40] S. Raghavan, S. Khan, Shear-thickening response of fumed silica suspensions under steady and oscillatory shear, J. Colloid and Interface Sci. 185 (1997) 57–67.

[41] M. Chellamuthu, E. Arndt, J. P. Rothstein, Extensional rheology of shear-thickening nanoparticle suspensions, Soft Matter 5 (2009) 2117–2124.

[42] P. M. Gresho, R. L. Sani, M. S. Engelman, Incompressible flow and the finite element method: Advection-diffusion and isothermal laminar flow, Wiley, 1998.

[43] S. R. Raghavan, S. A. Khan, Shear-induced microstructural changes in flocculated suspensions of fumed silica, J. Rheol. 39 (6) (1995) 1311–1325.

[44] F. J. Galindo-Rosales, Static and dynamic yield stresses of Aerosil® 200 suspension in polypropylene glycol, Applied Rheology.

[45] N. J. Wagner, J. F. Brady, Shear thickening in colloidal dispersions, Physics Today 62 (10) (2009) 27–32.

[46] S. R. Raghavan, H. J. Walls, S. A. Khan, Rheology of silica dispersions in organic liquids:Ä new evidence for solvation forces dictated by hydrogen bonding, Langmuir 16 (21) (2000) 7920–7930.

[47] F. J. Galindo-Rosales, F. J. Rubio-Hernández, A. Sevilla, An apparent viscosity function for shear thickening fluids, J. Non-Newtonian Fluid Mech. 166 (5-6) (2011) 321–325.

[48] A. Bhardwaj, E. Miller, J. P. Rothstein, Filament stretching and capillary breakup extensional rheometry measurements of viscoelastic wormlike micelle solutions, J. Rheol. 51 (4) (2007) 693–719.

[49] S. H. Spiegelberg, D. C. Ables, G. H. McKinley, The role of end-effects on measurements of extensional viscosity in filament stretching rheometers, J. Non-Newtonian Fluid Mech. 64 (2–3) (1996) 229–267.

[50] J. P. Rothstein, G. H. McKinley, A comparison of the stress and birefringence growth of dilute, semi-dilute and concentrated polymer solutions in uniaxial extensional flows, J. Non-Newtonian Fluid Mech. 108 (2136) (2002) 275–290.

[51] J. P. Rothstein, G. H. McKinley, Inhomogeneous transient uniaxial extensional rheometry, J. Rheol. 46 (6) (2002) 1419–1443.

[52] P. Szabo, Transient filament stretching rheometer I: Force balance analysis, Rheol. Acta 36 (1997) 277–284.

[53] S. Khandavalli, J. Rothstein, Extensional rheology of shear-thickening nanoparticle dispersions in an aqueous polyethylene oxide solutions, J. Rheol. 58 (2) (2014) 411–431.

[54] J. Wang, R. Bai, D. D. Joseph, Nanoparticle-laden tubeless and open siphons, J. Fluid Mech. 516 (2004) 335–348.

[55] L. Martinie, H. Buggisch, N. Willenbacher, Apparent elongational yield stress of soft matter, J. Rheol. 57 (2) (2013) 627–646.

[56] J. Boujlel, P. Coussot, Measuring the surface tension of yield stress fluids, Soft Matter 9 (2013) 5898–5908.

[57] J. E. Sprittles, Y. D. Shikhmurzaev, Finite element framework for describing dynamic wetting phenomena, Int. J. Numer. Meth. Fluids 68 (10) (2011) 1257–1298.

[58] J. G. Petrov, J. Ralston, M. Schneemilch, R. A. Hayes, Dynamics of partial wetting and dewetting in well-defined systems, J Phys. Chem. B 107 (7) (2003) 1634–1645.

[59] T. D. Blake, The physics of moving wetting lines, J. Colloid Interface Sci. 299 (1) (2006) 1–13.

[60] Y. D. Shikhmurzaev, Dynamic contact angles and flow in vicinity of moving contact line, AIChE Journal 42 (3) (1996) 601–612.